



Synthesis of novel $\text{Bi}_{0.5}\text{Na}_{0.5}\text{Ti}_{0.95}(\text{Ni}_{0.2}\text{Fe}_{0.2}\text{Sb}_{0.6})_{0.05}\text{O}_3$ perovskite material used as a photocatalyst for methylene blue degradation under sunlight irradiation

Rahima Rahal¹ · Malika Abba¹ · Zelikha Necira² · Salah Eddine Hachani³ · Achouak Achour¹ · Abdelhek Meklid² · Asma Dahri⁴ · Samir Kenouche² · Derradji Sahnoune⁵

Received: 24 March 2024 / Accepted: 21 April 2024 / Published online: 3 June 2024
© Akadémiai Kiadó, Budapest, Hungary 2024

Abstract

In this study, we synthesized a novel ceramic material $\text{Bi}_{0.5}\text{Na}_{0.5}\text{Ti}_{0.95}(\text{Ni}_{0.2}\text{Fe}_{0.2}\text{Sb}_{0.6})_{0.05}\text{O}_3$ named BNT-NFS via the solid-state route and assessed its efficacy as a photocatalyst for removing methylene blue dye from wastewater. The synthesized samples underwent thorough characterization using thermogravimetric analysis combined differential thermal analysis TGA-TDA, X-ray diffraction (XRD), Fourier-transform infrared spectroscopy (FTIR), scanning electron microscopy (SEM), Brunauer-Emmett-Teller (BET) analysis, and UV–Visible measurements. TGA-DTA and XRD analyses confirmed the successful formation of BNT-NFS material at 1150 °C, exhibiting a hexagonal phase structure. FTIR analysis revealed an intense band at 421 cm^{-1} , corresponding to metal-oxide vibrations in the BNT-NFS spectrum. SEM observations unveiled a distinct microstructure of BNT-NFS composed of grains of varying sizes. BET analysis indicated that the prepared BNT-NFS powder possessed a significant specific surface area of 261.36 m^2/g . Optical and photocatalytic assessments demonstrated that BNT-NFS perovskite is a semiconductor material with a band gap of 2.73 eV, exhibiting satisfactory photocatalytic activity for methylene blue MB dye removal. Notably, the removal efficiency reached 60% after 210 min of exposure to sunlight irradiation. This result is better than that registered for the pristine BNT.

Keywords BNT-NFS · Solid-state route · Photocatalytic · MB · Dye · Sunlight irradiation

Introduction

Dyes have various applications in our daily life, ranging from coloring textiles, foods, cosmetics, and pharmaceuticals to being used in the printing industry and in various art and craft projects [1]. However, while dyes serve important purposes, there are also potential harms associated with their use including skin irritation, respiratory problems, and even toxicity upon exposure through ingestion, inhalation, or skin absorption [2]. Environmental impacts include water pollution from untreated dye effluents, soil contamination due to improper waste disposal, and air pollution from dyeing processes. Additionally, the production of synthetic dyes contributes to resource depletion and ecosystem disturbance, as dyes discharged into water bodies can disrupt aquatic ecosystems and accumulate in soil, affecting microbial communities and nutrient cycles [3]. These concerns underscore the imperative for adopting sustainable practices in dye production, usage, and disposal to mitigate adverse health and environmental effects.

Treating dyes from wastewater involves a combination of biological and chemical methods to efficiently eliminate dye contaminants. Biological treatment methods, including the activated sludge process, constructed wetlands, and bioremediation, utilize microorganisms or natural ecosystems to degrade organic pollutants, breaking down dye molecules into simpler compounds [4]. Chemical treatment techniques like coagulation and flocculation, adsorption [5], and advanced oxidation processes target dye removal by destabilizing dye molecules, attaching them to solid surfaces, or oxidizing them into harmless byproducts using reactive radicals. These methods offer diverse approaches for addressing dye wastewater, considering factors like dye type, concentration, and environmental impact [6].

Photocatalysis stands out as a highly promising and environmentally friendly approach for treating dye-contaminated wastewater owing to its inherent simplicity, cost-effectiveness, and the absence of secondary metabolites that could potentially pose risks to the environment or human health [7].

In greater detail, photocatalysis involves the utilization of semiconductor materials which serve as the photocatalysts in the treatment system. Upon absorption of photons from the incident light, the semiconductor photocatalyst undergoes electronic excitation, generating electron–hole pairs within its structure. These photoinduced charge carriers then interact with dissolved oxygen or water molecules present in the surrounding medium, leading to the formation of highly reactive oxygen species such as hydroxyl radicals ($\bullet\text{OH}$) and superoxide radicals ($\text{O}_2\bullet^-$) act as potent oxidizing agents, initiating a cascade of chemical reactions wherein they attack and degrade the targeted dye molecules present in the wastewater into smaller, harmless, non-toxic byproducts such as carbon dioxide (CO_2) and water (H_2O), thereby mitigating the environmental and health risks associated with dye pollution [8].

Both pure and doped semiconductors are valuable in photocatalysis for their ability to harness light energy to drive chemical reactions. While pure semiconductors like serve as efficient photocatalysts, doping strategies enhance their photocatalytic performance by modifying their electronic and optical properties, thus

expanding their applicability in environmental remediation and sustainable technology development [9].

Perovskite materials have a specific crystal structure characterized by the general formula ABO_3 have emerged as promising candidates for photocatalysis due to their unique properties, including excellent light absorption, charge carrier mobility, and catalytic activity [10]. Bismuth sodium titanate based perovskite BNT photocatalysts have garnered significant attention in recent years due to their unique properties and potential applications in photocatalysis [11, 12]. Researchers are actively exploring strategies to enhance the photocatalytic activity of BNT-based perovskite photocatalysts. This includes doping with various elements to modify the electronic band structure, surface properties, and charge carrier dynamics of BNT, thereby improving its efficiency in photocatalytic reactions [13].

As far as current research indicates, there has yet to be a dedicated scientific investigation into the impact of multiple doping involving nickel (Ni), iron (Fe), and antimony (Sb) chemical elements on the properties of BNT ceramic material, particularly focusing on its photocatalytic properties. This unexplored area represents a significant gap in the existing body of knowledge regarding the potential enhancements or alterations that such multi-element doping could impart to the unique characteristics and functionalities of BNT-based materials, especially in the realm of photocatalysis.

This scientific contribution aims to develop a novel photocatalyst utilizing BNT ceramic powder doped with nickel (Ni), iron (Fe), and antimony (Sb) oxides, denoted by the chemical formula $Bi_{0.5}Na_{0.5}Ti_{0.95}(Ni_{0.2}Fe_{0.2}Sb_{0.6})_{0.05}O_3$, through the solid-state reaction method. The study begins with the analysis of the prepared precursor using TGA/DTA and XRD techniques to determine the optimal calcination temperature. Subsequently, the structural, morphological, and surface properties of the prepared photocatalyst powder are investigated through X-rays diffraction XRD, Fourier transform infrared spectroscopy FTIR, scanning electron microscopy SEM, and Raman analyzes. Furthermore, UV–Visible spectroscopy measurements are conducted to evaluate the band gap energy and the photocatalytic efficacy of the photocatalyst in terms of degrading blue methylene, a representative water contaminant used in the study. This comprehensive approach allows for a thorough understanding of the newly developed photocatalyst characteristics and its potential for environmental remediation applications.

Experimental part

Photocatalyst synthesis

The synthesis of $Bi_{0.5}Na_{0.5}Ti_{0.95}(Ni_{0.2}Fe_{0.2}Sb_{0.6})_{0.05}O_3$ ceramic powder, referred to as BNT-NFS, was achieved through the solid-state method, employing highly pure Bi_2O_3 (99% purity, BIOCHEM), Na_2CO_3 (99% purity, BIOCHEM), TiO_2 (99% purity, BIOCHEM), NiO (99% purity, BIOCHEM), Fe_2O_3 (99% purity, BIOCHEM), and Sb_2O_3 (99% purity, BIOCHEM) as the primary starting materials. To initiate the synthesis, stoichiometric amounts of these oxides were dissolved in ethanol solvent

and meticulously mixed under magnetic stirring at 80 °C for duration of 4 h. Following this, the mixture underwent a drying process at 100 °C for 24 h to eliminate any remaining traces of the solvent. Subsequently, the resulting mixture was subjected to grinding for 4 h using an agate mortar, followed by a meticulous calcination process at 1150 °C for 6 h in a laboratory oven, employing a controlled heating rate of 2 °C/min. Prior to various analyses, the calcined powder was further milled to obtain a fine powder consistency, ensuring optimal conditions for subsequent characterization and evaluation.

Characterizations

The precursor sample underwent DTA-TGA analysis to explore the mechanism underlying the formation of the BNT-FNS phase. A sample weighing 18.03 mg underwent heating from 40 to 1200 °C at a rate of 5 °C/min under a nitrogen atmosphere using the SETARAM Labsys Evo-gas option machine. For phase identification, X-ray diffraction (XRD) testing was conducted on powder samples, registering data across Bragg angles ranging from 10 to 90° using the EMPYREAN instrument. Structural properties of the prepared BNT-FNS photocatalyst powder were examined via FTIR analysis, where a 40 mg sample was pressed into a thin pellet suitable for measurement. FTIR scans were recorded over wavenumbers ranging from 400 to 4000 cm^{-1} using the Shimadzu spectrometer model 8400. Surface properties, including surface area and pore volume, were determined using the BET method with a ASIQUIN Quantachrome device operating with nitrogen (N_2). Morphological assessment of the BNT-FNS powder was conducted using scanning electron microscopy (SEM) with a TESCAN VEGA3 operating at a voltage of 20 kV under low vacuum conditions. Structural properties of the BNT-FNS were further investigated using Raman spectroscopy employing a micro-Raman spectrometer, specifically the Horiba LabRAM HRT 4600 HR800. Lastly, the optical and photocatalytic properties of the BNT-FNS powder were evaluated using The Perkin Elmer Lambda 35 UV/VIS spectrophotometer. The photocatalytic activity of the samples was assessed by measuring the degradation of methylene blue (MB), chosen as a model pollutant due to its widespread presence in various industrial effluents. In a 100 ml flask photoreactor, 20 mg of the prepared BNT-FNS powder was added as the photocatalyst to a solution containing 10 mg/l of MB. Following a 60 min stirring period in darkness to achieve adsorption–desorption equilibrium, sunlight was utilized as the irradiation source. At 30 min intervals, samples were taken from the mixture, centrifuged, and filtered to eliminate particle residue, with the filtrate's concentration analyzed by measuring absorbance at $\lambda_{\text{max}} = 664 \text{ nm}$.

UV–Vis spectra were recorded periodically to monitor changes in the concentration of the organic dye under analysis. The absorbance (A_i) measured after 1 h of stirring in darkness served as the initial concentration (C_i) of the solution, while the absorbance (A_f) determined after various illumination periods represented the residual concentration (C_f). The degradation efficiency (DE) of the organic dye was calculated using the following equation [14]:

$$DE(\%) = \frac{C_i - C_f}{C_i} \times 100 \quad (1)$$

Results and discussion

DTA-TGA results

The resulting precursor has subjected to DTA-TGA analysis in order to explore its decomposition under nitrogen and with the aim of establishing the most adequate calcination conditions. Fig. 1 presents the DTA-TGA curves illustrating the thermal behavior of the tested sample. The TGA curve depicts a series of weight losses corresponding to three respective thermal regions. Initially, a weight loss of 7.357% occurs in the temperature range of 31.35–441.95 °C, attributed to the vaporization of water from the samples. Subsequently, a weight loss of 1.297% is observed between 441.12 and 599.24 °C, associated with the decomposition of the precursors. A further weight loss of 3.298% occurs in the range of 599.88 °C to 836.95 °C during the decarbonization process. Concomitant with decarbonization, the final solid–solid synthesis reaction takes place. While this reaction does not result in mass loss, it is characterized by a distinct endothermic peak at 836.95 °C. The clarity of this endothermic peak renders it a reliable indicator of the complete synthesis reaction of BNT-NFS, facilitating precise monitoring of the synthesis process [15].

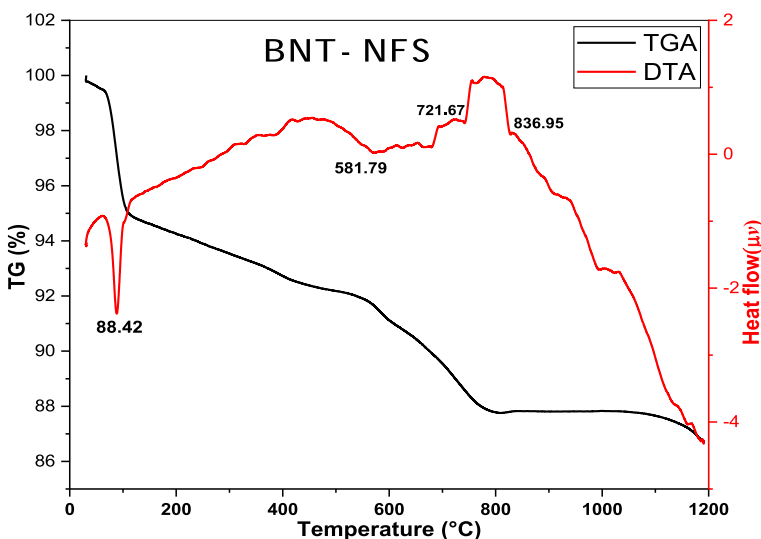


Fig. 1 DTA and TGA curves of the precursor used to elaborate BNT-NFS material under N₂ flushing over the temperature range from 40 to 1200 °C, with a heating rate of 5 °C/min

XRD outcomes

XRD analysis was conducted to ascertain phase identification in the studied samples, which were subjected to calcination ranging from 500 to 1150 °C to explore the mechanism behind BNT-NFS ceramic phase formation. The resulting XRD patterns were directly compared with those in the JCPDS database using the X'Pert High Score program package as exhibited in Fig. 2. The examination of the diffractograms from the sample calcined at 500 °C revealed distinct patterns indicating the presence of sodium carbonate Na_2CO_3 (00-037-0451), bismuth oxide Bi_2O_3 (01-072-0398), and titanium oxide TiO_2 varieties including anatase (98-004-4882) and rutile (98-005-1941).

Upon analyzing the XRD pattern of the sample calcined at 600 °C, the formation of the sillenite phase $\text{Bi}_{12}\text{TiO}_{20}$ (00-034-0097) mixed with the residue of the

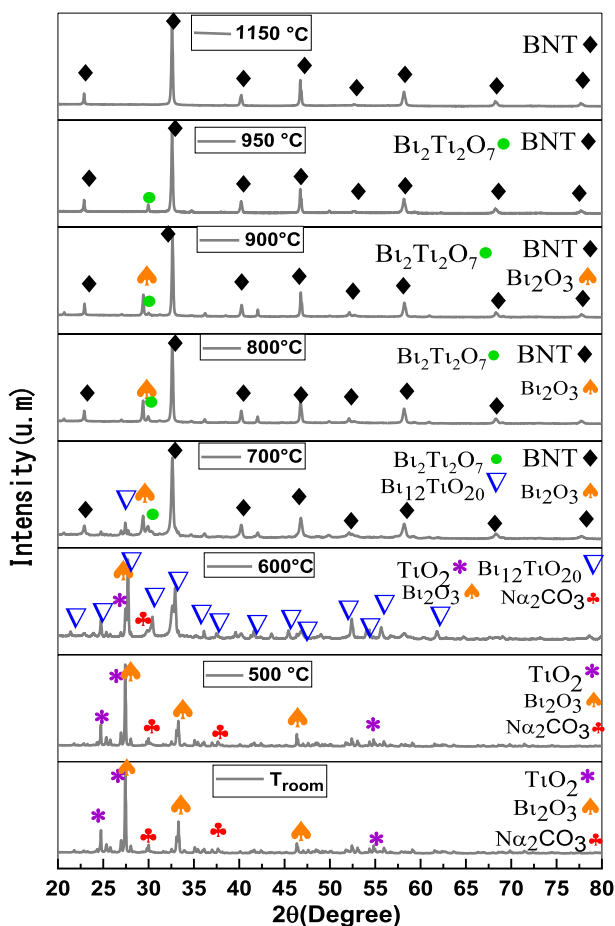
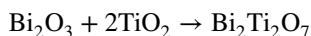


Fig. 2 XRD patterns of the precursor material at room temperature and following calcination in the 500–1150 °C range

compounds detected at 500 °C, consistent with findings by Zhou et al. [16]. Further examination of the XRD pattern of the sample calcined at 700 °C showed the formation of a powder composition comprising various phases, including $\text{Bi}_{0.5}\text{Na}_{0.5}\text{TiO}_3$ (00-046-0001), bismuth titanate pyrochlore $\text{Bi}_2\text{Ti}_2\text{O}_7$ (98-009-9436), sillenite $\text{Bi}_{12}\text{TiO}_{20}$ (00-034-0097), and bismuth oxide Bi_2O_3 (01-072-0398), aligning with previous studies on BNT ceramics [17]. The formation of bismuth titanate pyrochlore $\text{Bi}_2\text{Ti}_2\text{O}_7$ (98-009-9436) is described as by the following equation:



Analysis of XRD patterns from samples calcined at 800 °C and 900 °C showed the disappearance of $\text{Bi}_{12}\text{TiO}_{20}$, leading to the formation of a ternary system containing $\text{Bi}_{0.5}\text{Na}_{0.5}\text{TiO}_3$, $\text{Bi}_2\text{Ti}_2\text{O}_7$, and Bi_2O_3 phases.

Upon examining the XRD pattern of the sample calcined at 950 °C, the absence of Bi_2O_3 from the previous ternary system was noted. Peaks from the XRD pattern of the sample calcined at 1150 °C aligned well with those of $\text{Bi}_{0.5}\text{Na}_{0.5}\text{TiO}_3$, indicating the total diffusion of Ni, Fe, Sb elements in the hosting BNT matrix to successfully form BNT-NFS ceramic phase.

The integration of DTA-TGA and XRD results allowed us to track intermediate reactions leading to BNT-NFS formation, revealing these discernible phases:

- A water evaporation-related endothermic peak around 81.42 °C.
- An endothermic peak at approximately 582 °C signifying $\text{Bi}_{12}\text{TiO}_{20}$ development.
- An endothermic peak associated with monoclinic BNT formation at about 721 °C, coinciding with Bi_2O_3 structural alteration due to decarbonization.
- An endothermic peak at around 836 °C indicating hexagonal BNT generation.
- Hexagonal BNT formation commences at 900 °C and reaches 1150 °C to achieve a single-phase structure.

Phase identification was performed using the X'Pert HighScore software, comparing the X-ray diffraction (XRD) pattern of the studied sample with entries from the Inorganic Crystal Structure Database (ICSD). The XRD pattern was found to closely match that of ICSD card number 98-028-0983, confirming the presence of a pure perovskite structure crystallized in a rhombohedral lattice with the space group R3c.

To conduct detailed structural characterization, Rietveld refinement was employed, utilizing the advanced FullProf software package for X-ray diffraction (XRD) pattern analysis. The refinement process incorporated the pseudo-Voigt function to model peak shapes. Several parameters underwent adjustment during refinement, including the scale factor, detector zero-point, cell parameters, atomic positions, isotropic displacement parameter, occupancy rate, half-width parameters, profile shape factor parameter, preferred orientation, and background points.

The Rietveld refinement of the XRD pattern for the BNT-NFS sample as given in Fig. 3a reveals a remarkable alignment between observed and computed profiles, demonstrating an exceptional degree of concordance. This agreement is

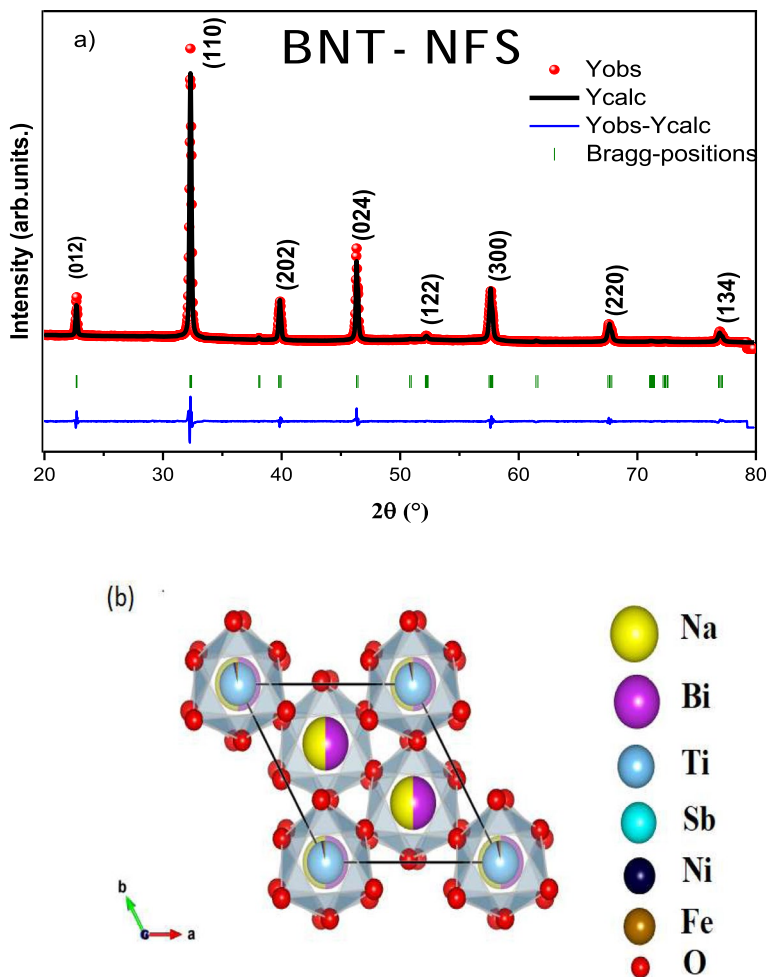


Fig. 3 **a** Rietveld refinement analysis of XRD pattern of BNT-NFS powder. **b** Crystal structures of the $\text{Bi}_{0.5}\text{Na}_{0.5}\text{Ti}_{0.95}(\text{Ni}_{0.2}\text{Fe}_{0.2}\text{Sb}_{0.6})_{0.05}\text{O}_3$ ceramic (hexagonal phase)

highlighted by significantly low χ^2 values and minimal Rp and RWp parameters, emphasizing the robust alignment achieved between observed and calculated datasets. The refined lattice parameters, as summarized in Table 1, validate the presence of a pristine perovskite structure within the sample, thereby affirming the credibility and accuracy of the experimental outcomes. This precision underscores the reliability of the fitting procedure in capturing the intricacies of the experimental findings.

Table 1 Refined parameters of BNT-NFS obtained through Rietveld refinement

$\text{Bi}_{0.5}\text{Na}_{0.5}\text{Ti}_{0.95}(\text{Ni}_{0.2}\text{Fe}_{0.2}\text{Sb}_{0.6})_{0.05}\text{O}_3$					
Crystal system	Hexagonal				
Space group	R 3 c				
Crystallographic parameters (\AA)	$a = b = 5.5349$, $c = 13.5949$, $\alpha = \beta = 90^\circ$, $\gamma = 120^\circ$				
V (volume) (\AA^3)	360.6890				
Atom position	Atom	X	Y	Z	
	O4	O	0.15121	0.35133	0.05827
	Ti3	Ti	0.00000	0.00000	0.00690
	Ni	Ni	0.00000	0.00000	0.00690
	Fe	Fe	0.00000	0.00000	0.00690
	Sb	Sb	0.00000	0.00000	0.00690
	Bi2	Bi	0.00000	0.00000	0.24580
	Na1	Na	0.00000	0.00000	0.24580
Rietveld factors	$R_p = 3.35$, $R_{wp} = 4.28$, $R_{exp} = 4.11$, $\chi^2 = 1.09$				
Theoretical density ρ_{th} (g/cm^3)	5.852				
Experimental density ρ_m (g/cm^3)	5.86				
Crystallite size (nm)	46.37				

FTIR results

Fig. 4 displays the Fourier Transform Infrared (FTIR) spectrum of the BNT-NFS sample. The spectrum exhibits prominent band peaks at 421, 672, and 815 cm^{-1} . Specifically, the band at 421 cm^{-1} corresponds to the metal-oxide vibrations within

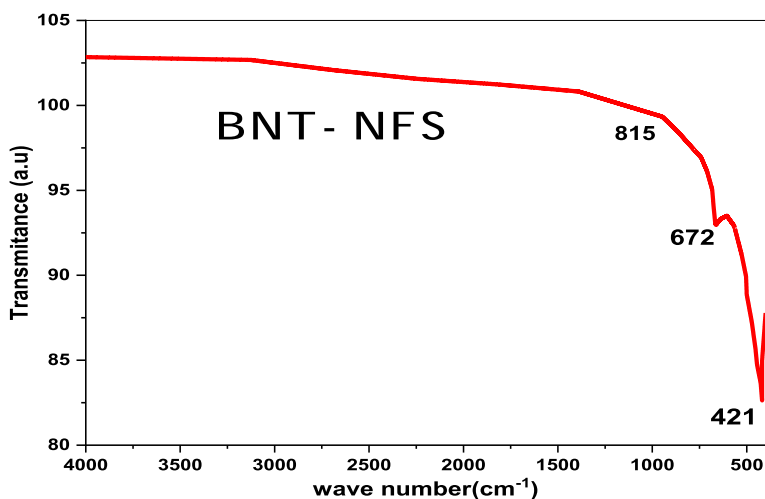


Fig. 4 FTIR spectrum of the prepared BNT-NFS sample, sample includes three distinct peaks at 421 cm^{-1} , 672 cm^{-1} , and 815 cm^{-1} .

the perovskite structure [18]. On the other hand, the bands observed at 672 and 815 cm^{-1} are attributed to the TiO_6 octahedra vibrations.

Raman results

Raman spectroscopy serves as a powerful tool for investigating structural changes at a microscale and within a limited timeframe. It complements XRD data and provides a more comprehensive understanding of structural transformations across different compositions [19]. Raman spectrum presented in Fig. 5 showcases six distinct vibrational modes of BNT-NFS, occurring at 78, 137, 287, 553, 824, and 854 cm^{-1} . These findings are consistent with previously published research [20–25]. Notably, Bi–O (78 cm^{-1}) and Na–O (137 cm^{-1}) exhibit A-site cation bonding in region I, typically around 200 cm^{-1} (low wavenumber) [26, 27]. This peak splitting suggests the presence of two distinct forms of A- BO_6 interactions within the NBT system. The 200–400 cm^{-1} mid-wavenumber range is presumed to correspond to Ti–O vibrations, while the 400–800 cm^{-1} high wavenumber range likely involves rotations and vibrations of oxygen octahedrals [28]. Two bands overlapping at approximately 800 cm^{-1} are linked to the longitudinal optical modes A1 and E in the high-frequency range [29, 30].

BET results

In Fig. 6, the adsorption–desorption isotherms of N_2 for the BNT-NFS sample under study are depicted. The BET studies conducted on the BNT-NFS particles revealed a type II+IV isotherm, indicative of their mesoporous and macroporous mixed nature. The specific surface area of the BNT-NFS powder was

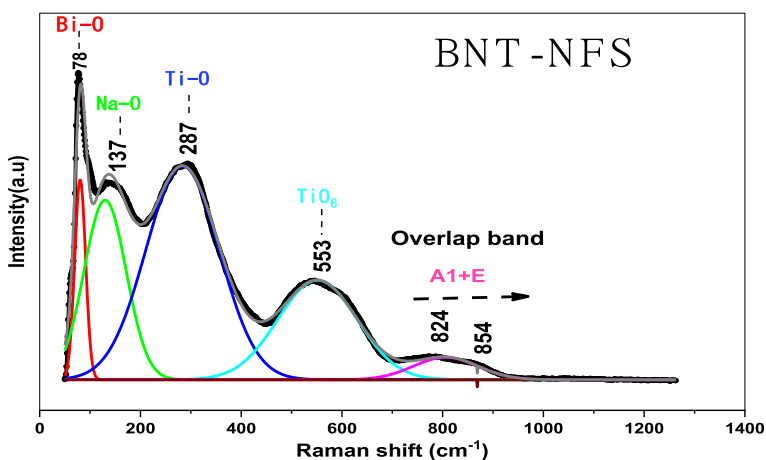


Fig. 5 Raman spectrum of BNT-NFS ceramic material, sample includes six distinct peaks at 78 cm^{-1} , 137 cm^{-1} , 287 cm^{-1} , 553 cm^{-1} , 824 cm^{-1} , and 854 cm^{-1}

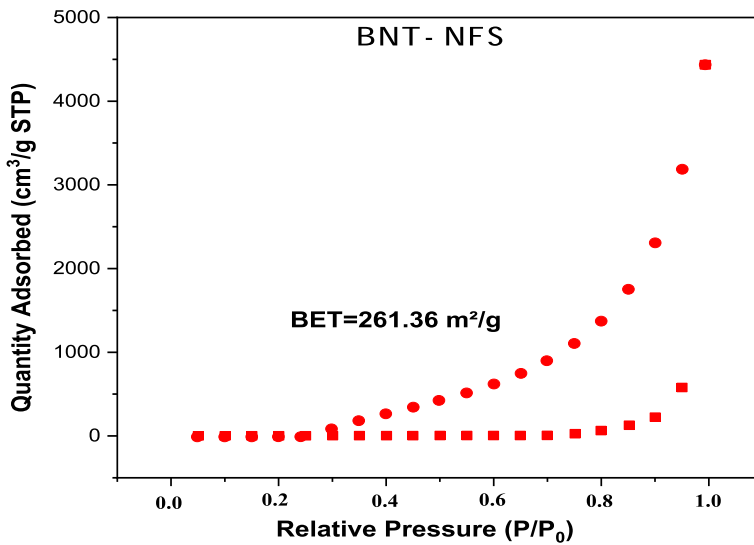


Fig. 6 N₂ adsorption–desorption isotherms of BNT-NFS sample with surface area equal to 261.36 m²/g

determined to be 261,36 m²/g indicating its considerable potential for various catalytic applications, particularly in photocatalysis.

SEM outcomes

The microstructure of a material is pivotal in defining a wide range of its properties, encompassing strength, toughness, hardness, wear resistance, ductility, formability, corrosion resistance, thermal and electrical conductivity, as well as optical and catalytic properties. Specifically regarding photocatalytic behavior, the microstructure assumes a critical role by influencing factors such as surface area, porosity, dopants, and morphology, including size, shape, and surface features. Materials with highly porous structures offer significant surface area, enhancing their photocatalytic potential. Consequently, Understanding and controlling the microstructure of photocatalysts are therefore essential for designing and optimizing materials with enhanced photocatalytic activity for various environmental and energy applications.

Fig. 7 showcases a scanning electron microscope (SEM) image capturing the microstructure of the BNT-NFS sample post-sintering at 1150 °C. The morphology exhibited by the sample is characterized by a notably high level of density. An intriguing observation lies in the significant diversity in grain size, evident from the coexistence of both larger and smaller grains throughout the sample. Moreover, utilizing “Image J software” for analysis revealed an average particle size of 4.59 μm, further underscoring the intricate characteristics of the sample’s microstructure.

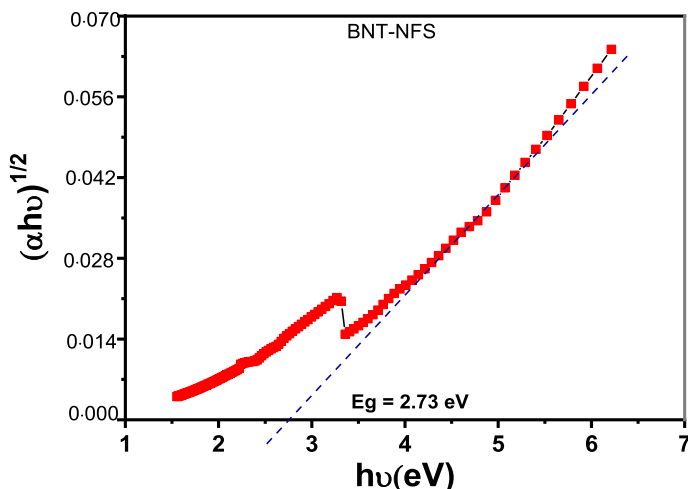


Fig. 7 Photon energy $h\nu$ dependent $(\alpha h\nu)^2$ of BNT-NFS with bandgap energy of approximately 2.73 eV

Optical properties

The band gap energy (E_g) of the tested BNT-NFS material was determined using the Tauc equation, represented by Eq. 2 [31]:

$$(\alpha h\nu)^n = A(h\nu - E_g) \quad (2)$$

In this equation, h , α , ν , and A correspond to Planck's constant, the absorption coefficient, the frequency of light, and a constant, respectively. The parameter n represents the Tauc exponent, which varies based on the type of electronic transition. For instance, $n=1/2$ is typical for direct allowed transitions, $n=2$ for indirect allowed transitions, and other values may apply to different transition types.

Fig. 8 illustrates the relationship between $(\alpha h\nu)^{1/2}$ and $h\nu$ energy. Extrapolating this plot provides an estimated E_g value of 2.73 eV, indicating the band gap energy of the BNT-NFS material under investigation. This result unequivocally signifies the semiconductor characteristics of the material under examination, albeit lower than that of the pure BNT [32]. Such findings underscore the substantial potential of this system as a photoactive material.

Photocatalytic study of the prepared BNT-NFS material

The photocatalytic activity of BNT-NFS powder was evaluated using methylene blue (MB) dye as a model contaminant. A solution containing 10 mg of BNT-NFS in distilled water as a solvent was subjected to sunlight irradiation. In Fig. 9, the variation in MB absorbance over time under sunlight irradiation is illustrated. It was observed that the main absorbance peak associated with MB decreased from 1.1 to

Fig. 8 SEM image of the obtained BNT-NFS material prepared by solid-state (SS) method at a temperature of 1150 °C

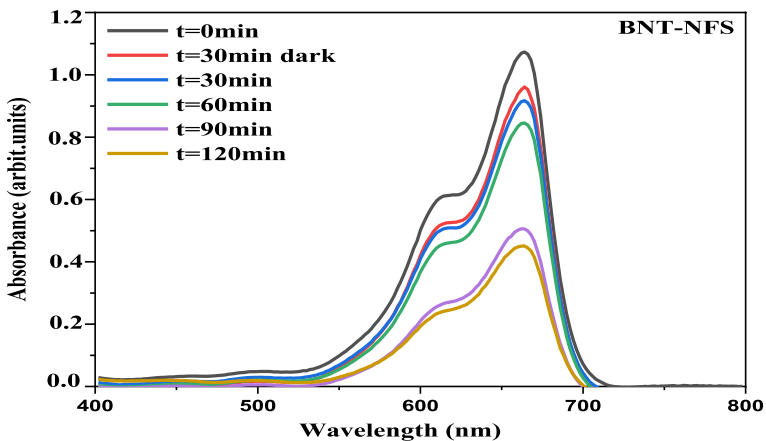
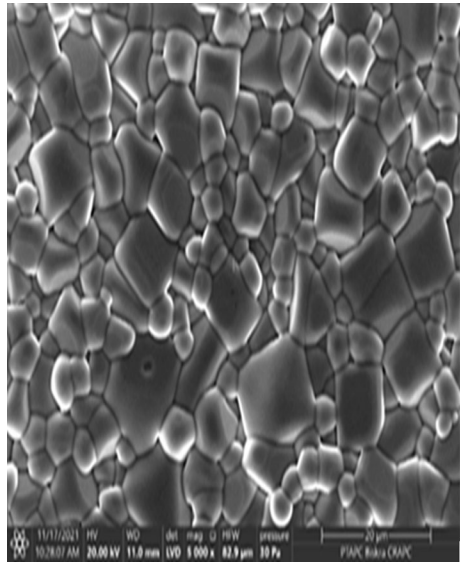


Fig. 9 UV–Visible spectra of photodegraded MB in the presence of BNT-NFS under sunlight irradiation ($C_0 = 10$ mg/l, $m_{\text{(BNT-NFS)}} = 0.1$ g, $T = 25$ °C)

0.44 after 210 min of sunlight exposure, indicating photodegradation of the dye in the presence of BNT-NFS as a photocatalyst. This was corroborated by the gradual disappearance of the typical blue color of the MB dye over different time intervals of sunlight exposure.

Fig. 10 depicts the progression of photocatalytic degradation of MB dye in the presence of BNT-NFS particles under sunlight irradiation as a function of time. The results show that the removal efficiency of MB increased with prolonged exposure to sunlight. Specifically, the removal efficiency reached 60% after 210 min of sunlight

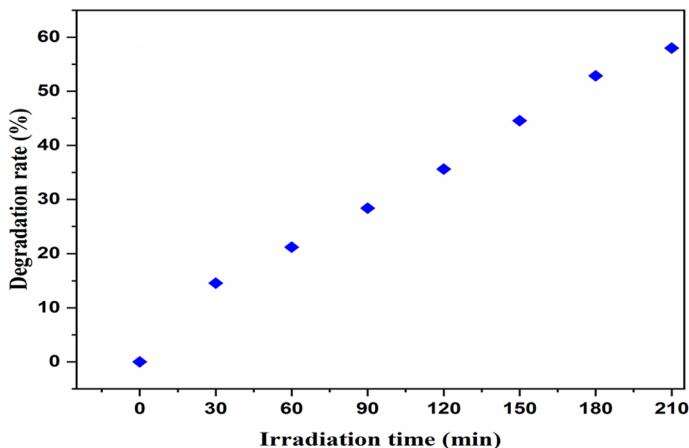


Fig. 10 The evolution of MB degradation as a function of time exposure to sunlight irradiation in the presence of BNT-NFS material ($C_0 = 10$ mg/l, $m_{\text{(BNT-NFS)}} = 0.1$ g, $T = 25$ °C)

irradiation. This result is better than that reported for the pure BNT having a degradation efficiency of 26%.

Conclusion

We have synthesized a novel perovskite system namely BNT-NFS as a photocatalyst to eliminate MB contaminant from wastewater. In the light of the above discussions, we can conclude that:

TGA-DTA and XRD results demonstrated that BNT-NFS solution has been successfully elaborated at 1150 °C. This material crystallized in hexagonal phase structure with R3c space group.

SEM images revealed that the microstructure of BNT-NFS material is compact and formed by grains of different sizes.

BET method demonstrated that BNT-NFS particles have an interesting surface area.

UV–visible analysis and absorbance measurements results confirmed that the prepared samples can be used as a good photocatalyst for MB degradation under sunlight irradiation with removal effectiveness reached 60%.

BNT-NFS exhibited higher photocatalytic activity compared to the pristine BNT material.

Supplementary Information The online version contains supplementary material available at <https://doi.org/10.1007/s11144-024-02635-9>.

Data availability The datasets analyzed during the current study are available from the corresponding author RAHAL Rahima on reasonable request.

References


1. Makhloufi R, Hachani SE, Zekri Z, Tair W (2022) Solvothermal synthesis of antimony trioxide Sb_2O_3 used as a photocatalyst for crystal violet dye degradation. *Mosc Univ Chem Bull* 77(2):111–116. <https://doi.org/10.3103/S0027131422020043>
2. Lellis B, Fávaro-Polonio CZ, Pamphile JA, Polonio JC (2019) Effects of textile dyes on health and the environment and bioremediation potential of living organisms. *Biotechnol Res Innov* 3(2):275–290. <https://doi.org/10.1016/j.biori.2019.09.001>
3. Al-Tohamy R, Ali SS, Li F, Okasha KM, Mahmoud YAG, Elsamahy T, Sun J (2022) A critical review on the treatment of dye-containing wastewater: ecotoxicological and health concerns of textile dyes and possible remediation approaches for environmental safety. *Ecotoxicol Environ Saf* 231:113160. <https://doi.org/10.1016/j.ecoenv.2021.113160>
4. Imran SM, Shao GN, Haider MS, Hwang HJ, Choa YH, Hussain M, Kim HT (2016) Carbon nanotube-based thermoplastic polyurethane-poly (methyl methacrylate) nanocomposites for pressure sensing applications. *Polym Eng Sci* 56(9):1031–1036. <https://doi.org/10.1002/polb.24333>
5. Ihaddaden S, Aberkane D, Boukerroui A, Robert D (2022) Removal of methylene blue (basic dye) by coagulation-flocculation with biomaterials (bentonite and *Opuntia ficus indica*). *J Water Process Eng* 49:102952. <https://doi.org/10.1016/j.jwpe.2022.102952>
6. Shahamat YD, Masihpour M, Borghei P, Rahmati SH (2022) Removal of azo red-60 dye by advanced oxidation process O₃/UV from textile wastewaters using Box-Behnken design. *Inorg Chem Commun* 143:109785. <https://doi.org/10.1016/j.inoche.2022.109785>
7. Makhloufi R, Hachani SE, Fettah A, Tair W, Zekri Z (2022) Synthesis of $\text{Sb}_2\text{S}_3\text{-Sb}_4\text{O}_5\text{Cl}_2$ composite used as a photocatalyst for crystal violet cationic dye degradation. *Chem Data Collect* 39:100867. <https://doi.org/10.1016/j.cdc.2022.100867>
8. Rajagopalan V (2016) A new synergetic nanocomposite for dye degradation in dark and light. *Sci Rep* 6(1):1–10. <https://doi.org/10.1038/srep38606>
9. Atalı ŞG, Akbal F, Gürbüz M, Turan BC (2023) Granular titanium dioxide and silicon-doped titanium dioxide as reusable photocatalysts for dye removal. *Int J Appl Ceram Technol*. <https://doi.org/10.1111/ijac.14603>
10. Dandia A, Saini P, Sharma R, Parewa V (2020) Visible light driven perovskite-based photocatalysts: a new candidate for green organic synthesis by photochemical protocol. *Curr Res Green Sustain Chem* 3:100031. <https://doi.org/10.1016/j.crgsc.2020.100031>
11. Zhou X, Sun Q, Zhai D, Xue G, Luo H, Zhang D (2021) Excellent catalytic performance of molten-salt-synthesized $\text{Bi}_{0.5}\text{Na}_{0.5}\text{TiO}_3$ nanorods by the piezo-phototronic coupling effect. *Nano Energy*. <https://doi.org/10.1016/j.nanoen.2021.105936>
12. Zhu C, Cai Z, Luo B, Guo L, Li L, Wang X (2020) High temperature lead-free BNT-based ceramics with stable energy storage and dielectric properties. *J Mater Chem A* 8(2):683–692. <https://doi.org/10.1039/C9TA10347C>
13. Kushwaha HS, Halder A, Jain D, Vaish R (2015) Visible light-induced photocatalytic and antibacterial activity of Li-doped $\text{Bi}_{0.5}\text{Na}_{0.45}\text{K}_{0.05}\text{TiO}_3\text{-BaTiO}_3$ ferroelectric ceramics. *J Electron Mater* 44:4334–4342. <https://doi.org/10.1007/s11664-015-4007-y>
14. Popoola LT, Yusuff AS, Adejare AT, Olasupo SB (2024) Photocatalytic degradation of methylene blue dye by magnetized $\text{TiO}_2\text{-silica}$ nanoparticles from rice husk. *Appl Water Sci* 14(2):25. <https://doi.org/10.1007/s13201-023-02052-8>
15. Yoon MS, Khansur NH, Ur SC (2010) The effect of pre-milling/presynthesis process and excess Ba on the microstructure and dielectric/piezoelectric properties of nano-sized $0.94[(\text{Bi}_{0.5}\text{Na}_{0.5})\text{TiO}_3]\text{-}0.06[\text{Ba}_{(1-x)}\text{TiO}_3]$. *Ceram Int* 36(4):1265–1275. <https://doi.org/10.1016/j.ceramint.2010.01.011>
16. Zhou J, Zou Z, Ray AK, Zhao XS (2007) Preparation and characterization of polycrystalline bismuth titanate $\text{Bi}_{12}\text{Ti}_{20}$ and its photocatalytic properties under visible light irradiation. *Ind Eng Chem Res* 46(3):745–749. <https://doi.org/10.1021/ie0613220>
17. Kang DH, Kang YH (2013) Dielectric and pyroelectric properties of lead-free sodium bismuth titanate thin films due to excess sodium and bismuth addition. *J Microelectron Packaging Soc* 20(4):25–30. <https://doi.org/10.6117/kmepps.2013.20.4.025>
18. Banerjee P, Franco A Jr (2017) Substitution-induced near phase transition with Maxwell-Wagner polarization in $\text{SrBi}_2(\text{Nb}_{1-x}\text{Ax})_2\text{O}_9$ ceramics [A= W, Mo and x= 0, 0.025]. *Phys Status Solid* 214(10):1700067. <https://doi.org/10.1002/pssa.201700067>

19. Rubio-Marcos F, Bañares MA, Romero JJ, Fernandez JF (2011) Correlation between the piezoelectric properties and the structure of lead-free KNN-modified ceramics, studied by Raman Spectroscopy. *J Raman Spectrosc* 42(4):639–643. <https://doi.org/10.1002/jrs.2753>
20. Zannen M, Lahmar A, Dietze M, Khemakhem H, Kabadou A, Es-Souni M (2012) Structural, optical, and electrical properties of Nd-doped $\text{Na}_{0.5}\text{Bi}_{0.5}\text{TiO}_3$. *Mater Chem Phys* 134(2–3):829–833. <https://doi.org/10.1016/j.matchemphys.2012.03.076>
21. Zhang MS, Scott JF (1986) *Ferroelectr Lett* 6:147–152. <https://doi.org/10.1080/07315178608200490>
22. Said S, Marchet P, Merle-Méjean T, Mercurio JP (2004) Raman spectroscopy study of the $\text{Na}_{0.5}\text{Bi}_{0.5}\text{TiO}_3$ – PbTiO_3 system. *Mater Lett* 58(9):1405–1409. <https://doi.org/10.1016/j.matlet.2003.09.036>
23. Kreisel J, Glazer AM, Jones G, Thomas PA, Abello L, Lucazeau G (2000) An x-ray diffraction and Raman spectroscopy investigation of A-site substituted perovskite compounds: the $(\text{Na}_{1-x}\text{K}_x)_{0.5}\text{Bi}_{0.5}\text{TiO}_3$ (0 < x < 1) solid solution. *J Phys Condens Matter* 12(14):3267. <https://doi.org/10.1088/0953-8984/12/14/305>
24. Siny IG, Husson E, Beny JM, Lushnikov SG, Rogacheva EA, Syrnikov PP (2000) Raman scattering in the relaxor-type ferroelectric Na1/2Bi1/2TiO_3 . *Ferroelectrics* 248(1):57–78. <https://doi.org/10.1080/00150190008223669>
25. Petzelt J, Kamba S, Fabry J, Noujmi D, Porokhonsky V, Pashkin A, Kugel GE (2004) Infrared, Raman and high-frequency dielectric spectroscopy and the phase transitions in Na1/2Bi1/2TiO_3 . *J Phys Condens Matter* 16(15):2719. <https://doi.org/10.1080/00150190008223669>
26. Raghavan CM, Kim JW, Song TK, Kim SS (2015) Microstructural and ferroelectric properties of rare earth (Ce, Pr, and Tb)-doped $\text{Na}_{0.5}\text{Bi}_{4.5}\text{Ti}_3\text{O}_{15}$ thin films. *Appl Surf Sci* 355:1007–1012. <https://doi.org/10.1016/j.apsusc.2015.07.199>
27. Swain S, Ojha B, Mohanty S (2016) Structural, electrical and optical properties of Tb doped bismuth sodium titanate. *J Mater Sci: Mater Electron* 27:8693–8700. <https://doi.org/10.1007/s10854-016-4891-9>
28. Luo L, Ge W, Li J, Viehland D, Farley C, Bodnar R, Luo H (2011) Raman spectroscopic study of Na1/2Bi1/2TiO_3 -x% BaTiO_3 single crystals as a function of temperature and composition. *J Appl Phys*. <https://doi.org/10.1063/1.3587236>
29. Bai W, Bian Y, Hao J, Shen B, Zhai J (2013) The composition and temperature-dependent structure evolution and large strain response in $(1-x)(\text{Bi}_{0.5}\text{Na}_{0.5})\text{TiO}_{3-x}\text{Ba}(\text{Al}_{0.5}\text{Ta}_{0.5})\text{O}_3$ ceramics. *J Am Ceram Soc* 96(1):246–252. <https://doi.org/10.1111/jace.12039>
30. Rafiq MA, Maqbool A, Khan IH, Manzoor MU, Shuaib A, Hakeem AS (2020) A facile and cost-effective approach for the fabrication $\text{Bi}_{0.5}\text{Na}_{0.5}\text{TiO}_3$ thick films on flexible substrate for energy storage capacitor applications. *Ceram Int* 46(16):25113–25121. <https://doi.org/10.1016/j.ceramint.2020.06.298>
31. Smaili L, Menasra H, Benbrika C, Ben Khetta O, Necira Z, Bounab K (2023) Enhanced photocatalytic degradation of Rhodamine B by (Mg/Ta): doped $\text{Bi}_4\text{Ti}_3\text{O}_{12}$ catalyst under sunlight irradiation. *React Kinet Mech Catal* 136(6):3257–3269. <https://doi.org/10.1007/s11144-023-02485-x>
32. Paul Blessington SA, Pazhnieluv V, Vasanth BK, Jagadeeshwaran C, Murugaraj R (2015) Investigation of structural and optical spectroscopy of 5% Pr doped $(\text{Bi}_{0.5}\text{Na}_{0.5})\text{TiO}_3$ ferroelectric ceramics: site depended study. *J Mater Sci Mater Electron* 26:7655–7665. <https://doi.org/10.1007/s10854-015-3405-5>

Publisher's Note Springer Nature remains neutral with regard to jurisdictional claims in published maps and institutional affiliations.

Springer Nature or its licensor (e.g. a society or other partner) holds exclusive rights to this article under a publishing agreement with the author(s) or other rightsholder(s); author self-archiving of the accepted manuscript version of this article is solely governed by the terms of such publishing agreement and applicable law.

Authors and Affiliations

Rahima Rahal¹  · **Malika Abba¹** · **Zelikha Necira²** · **Salah Eddine Hachani³** · **Achouak Achour¹** · **Abdelhek Meklid²** · **Asma Dahri⁴** · **Samir Kenouche²** · **Derradji Sahnoune⁵**

✉ Rahima Rahal
rahima.rahal@univ-biskra.dz

- ¹ Laboratory of Molecular Chemistry and Environment, University of Biskra, B. P. 145, 07000 Biskra, Algeria
- ² Laboratory of Applied Chemistry, University of Biskra, B. P. 145, 07000 Biskra, Algeria
- ³ Department of Process Engineering and Petrochemistry, Faculty of Technology, University of El Oued, 39000 El Oued, Algeria
- ⁴ Laboratory of Multifunctional Materials and Applications (LaMMA), Faculty of Sciences of Sfax, University of Sfax, BP 1171, 3000 Sfax, Tunisia
- ⁵ Scientific and Technical Research Centre in Physicochemical Analyses CRAPC, PTAPC, Biskra, Algeria